Applied Energy 212 (2018) 919–930

Contents lists available at ScienceDirect

Applied Energy

journal homepage: www.elsevier.com/locate/apenergy

Control development and performance evaluation for battery/flywheel hybrid energy storage solutions to mitigate load fluctuations in all-electric ship propulsion systems

Jun Hou[a,*], Jing Sun[a,b], Heath Hofmann[a]

[a] Department of Electrical Engineering and Computer Science, University of Michigan, Ann Arbor, MI 48109, USA
[b] Department of Naval Architecture and Marine Engineering, University of Michigan, Ann Arbor, MI 48109, USA

HIGHLIGHTS

- A new B/FW HESS is proposed to isolate load fluctuations from the shipboard network.
- A periodic DP algorithm is developed to reduce the computational cost.
- A comparative study illustrates the advantages and limitations of B/UC and B/FW HESS.
- A novel MPC-based approach is developed to facilitate real-time implementation.
- The proposed MPC is validated in a laboratory-scaled experiment.

ARTICLE INFO

Keywords:
Electric ship propulsion
Hybrid energy storage
Multi-objective optimization
Model predictive control
Energy management
Dynamic programming

ABSTRACT

Current trends in both commercial and military ship development have focused on ship electrification. A challenge for electric-ship propulsion systems, however, is large propulsion-load fluctuations. To address this issue, this paper explores a new solution, namely a combined battery and flywheel (B/FW) hybrid energy storage system (HESS) as a buffer to isolate load fluctuations from the shipboard network. Our two main objectives, power-fluctuation compensation and energy saving under various operating constraints, are formulated as a multi-objective optimization problem. Pareto fronts, which illustrate the trade-offs between the main objectives, are obtained by using dynamic programming with the weighted sum method. To quantitatively analyze the performance of B/FW HESS, a comparative study is performed under different sea conditions, where a battery/ultra-capacitor (B/UC) HESS configuration is used as a reference in performance evaluation. Simulation results show the feasibility and effectiveness of B/FW to mitigate the load fluctuations for all-electric ships, especially at high sea states. Furthermore, a model predictive control (MPC) algorithm is developed to facilitate real-time implementation of the proposed solution. A performance comparison between the proposed MPC energy management strategy and the global dynamic programming is performed, and this comparison demonstrates the effectiveness of the proposed MPC strategy.

1. Introduction

Ship electrification has become a dominant trend for both commercial and military ship development to improve efficiency, reduce emissions, support high-power mission systems, and provide a more comfortable environment for crew and passengers [1–5]. The all-electric ship propulsion system provides new opportunities to solve old problems and develop new solutions. One of the classic problems is propulsion-load fluctuations, which are caused by the propeller rotation and encounter waves and can significantly affect both mechanical and electrical systems [6–9]. While the problem exists in conventional mechanical drivetrains, the resulting consequences of power fluctuations can be more pronounced for electrical propulsion systems. In addition to mechanical wear and tear caused by high-frequency unbalanced torque and speed oscillations, reliability and efficiency of shipboard power system can be negatively impacted. To address load fluctuations, several methods have been proposed, such as using thruster biasing for vessels with dynamic positioning systems [10]. This approach is mainly used for low-frequency fluctuations, and is applied to dynamic positioning systems. Another popular solution is to

* Corresponding author.
E-mail addresses: junhou@umich.edu (J. Hou), jingsun@umich.edu (J. Sun), hofmann@umich.edu (H. Hofmann).

https://doi.org/10.1016/j.apenergy.2017.12.098
Received 21 October 2017; Received in revised form 11 December 2017; Accepted 27 December 2017
Available online 04 January 2018
0306-2619/

incorporate an energy storage system (ESS) to smooth the load power [11–14]. Different combinations of ESSs should be considered for different applications [15–18]. Only using one single type of ESS can result in increased size, weight and cost for electric ship operations [19]. With multi-frequency characteristics of the propulsion-load fluctuations, a combination of battery packs and ultra-capacitor modules (B/UC) has been investigated and analyzed [20], where the complementary characteristics of B/UC hybrid energy storage system (HESS) have been exploited with properly coordinated control.

Besides ultra-capacitors and batteries, flywheels have been widely used as uninterruptible power supplies (UPS) [21], and for wind power smoothing [22,23], heavy haul locomotives [24] and frequency response [25]. The importance of flywheels for electrified ships has been mentioned in the Naval Power System Technology Development Roadmap [26]. In [27–29], flywheels were explored to address pulse power loads on the shipboard power network. Compared to batteries and ultra-capacitors (UC), flywheels offer an intermediate choice with respect to energy and power density. Note that the batteries investigated in this paper is lithium-ion batteries, which have higher power and energy densities than other batteries [30]. Flywheels have been enhanced with the development of magnetic bearings, which facilitates high-speed flywheels with significantly reduced the friction losses [31]. In general, flywheels provide a higher power density compared to batteries and a higher energy density compared to ultra-capacitors [32,33]. Furthermore, compared to batteries, flywheels have a long lifetime without capacity degradation, and the ability to operate over a much wider temperature range without performance degradation [31]. Given the considerable benefits of flywheels, we investigate the feasibility of a battery/flywheel (B/FW) HESS to mitigate the effect of propulsion-load fluctuations on the shipboard power network. The B/UC HESS solution proposed in [20] is used as a reference to demonstrate the advantages and limitations of the B/FW HESS solution.

In this paper, the potential of the B/FW HESS in counteracting load fluctuations is formulated as a multi-objective optimization problem (MOP). Two main objectives are power-fluctuation compensation and HESS loss minimization. Since these objectives conflict with each other in the sense that effective compensation of fluctuations will lead to HESS losses, the weighted-sum method is used to convert this MOP into a single-objective problem. Global optimal solutions are obtained using dynamic programming (DP) by exploiting the periodicity of the load. These global optimal solutions form the basis of a comparative study of B/FW and B/UC HESS, where the Pareto fronts of these two technologies at different sea state (SS) conditions are derived. The analysis aims to provide insights into the advantages and limitations of the B/FW HESS solution.

Due to the high computational cost, DP typically cannot be directly used for real-time applications. In order to enable real-time applications, rule-based control approaches abstracted from the optimization results with DP algorithm, have been explored in the literature [17,34,35]. Model predictive control (MPC) is another effective approach for energy management [36]. MPC is able to obtain the optimal solution and deal with constraints. Optimization-based energy management is also recommended in the Naval Power Systems Technology Development Roadmap [26]. Therefore, a MPC-based approach is developed in this paper. For nonlinear optimization problems, a short predictive horizon is preferred for real-time applications. However, the effectiveness of MPC could be limited by a short predictive horizon [17]. To enable real-time application and achieve desired performance, a novel MPC strategy is developed. In this MPC formulation, a state of charge (SOC) reference is used to address the limitations imposed by short predictive horizons.

This paper is built on our previous work presented at the 2017 IEEE American Control Conference [37]. However, this paper provides substantial new results by: (a) taking the battery nonlinear dynamics (SOC vs open circuit voltage) into consideration; (b) developing a dynamic programming algorithm based on a periodic load characteristic to obtain global optimal solutions (Pareto-fronts); (c) analyzing the Pareto-fronts of B/FW and B/UC at different sea states; and (d) evaluating the effectiveness of the proposed MPC strategy compared with the global optimal solutions. The contributions of this paper are summarized in the following:

- A new B/FW HESS configuration is proposed to deal with propulsion-load fluctuations from the shipboard network.
- To our best knowledge, this is the first study to quantitatively analyze the performance of two HESS configurations, namely B/UC and B/FW HESS, in addressing the multi-frequency propulsion-load fluctuation problem for all-electric ships. This study provides insights into the advantages and limitations of each configuration.
- A dynamic programming algorithm based on a periodic load characteristic is developed to reduce the required hardware memory and computational time.
- A novel MPC approach is developed to facilitate real-time implementation of the proposed solution. The proposed approach is validated in a laboratory-scaled experiment.

This paper is organized as follows. The control-oriented ship propulsion model is summarized and dynamic models of battery, flywheel and ultra-capacitor are described in Section 2. In Section 3, the key components of the B/FW and B/UC HESS are sized according to the frequency components of the load fluctuations at nominal sea state. In Section 4, the MOP is formulated and solved, and a comparison study between B/UC and B/FW is performed. In Section 5, an MPC strategy is developed and evaluated to enable real-time implementation. Section 6 concludes the paper.

2. Dynamic model of an electric ship propulsion system with hybrid energy storage

The models presented in this section were developed in [20,37] and will be essential for the performance analysis. The key elements of the model are presented in this section for easy reference, while details can be found in [20].

2.1. Propeller and ship dynamic model

The propeller and ship model captures the dynamic behavior of the propeller and ship motion, including the power and torque fluctuations induced on the motor drive shaft, and determines the power demand (P_{FL}) for the HESS. The mechanical load power transmitted to the ship body from the propeller can be expressed as:

$$P_{Load} = 2\pi nQ, \tag{1}$$

where Q is the propeller torque and n is the rotational speed of the propeller in revolutions-per second. The induction motor is assumed to be directly connected to the propeller (as typically done for all-electric ships), so n is also the rotational speed of the induction motor. The torque generated by the propeller can be expressed as:

$$Q = \mathrm{sgn}(n)\beta K_{Q0}\rho n^2 D^5, \tag{2}$$

where K_{Q0} denotes the torque coefficient when no losses are present, β is the loss factor, which is used to capture the effects of in-and-out water motion of the propeller, ρ is the density of water, and D is the diameter of the propeller. The torque coefficient is determined as follows:

$$K_{Q0} = f_{K_Q}(J, PR, A_e/A_o, Z, R_n), \tag{3}$$

where $J = \frac{V_a}{nD}$ is the advance coefficient with V_a being the ship advance speed, PR is the pitch ratio, A_e/A_0 is the expanded blade-area ratio, Z is the number of blades, and R_n is the Reynolds number. Note that the wake field, defined as , should be taken into account, which includes the average and fluctuation components.

The ship dynamics encompass the response of the ship speed U to

different forcing functions, including those from the propulsion system, wave excitations, wind, and hydrodynamic resistances [38,39]:

$$(m + m_x)\frac{dU}{dt} = T(1-t_d) + R + F, \tag{4}$$

where m is the mass of ship, m_x is the added-mass of the ship, t_d is the thrust deduction coefficient, F represents wave disturbances, R is the total resistance force including frictional resistance, wave-making resistance, and wind resistance, and T is the propeller thrust, which is defined as follows:

$$T = \mathrm{sgn}(n)\beta\rho n^2 D^4 f_{K_T}(J_A, Pitch/D, A_e/A_o, Z, R_n) \tag{5}$$

The wake field oscillation in w results in high-frequency fluctuations, and the wave effect leads to low-frequency fluctuations through the ship speed U and the in-and-out of water loss factor β.

2.2. Hybrid energy storage system model

For the B/FW HESS model, we define the states as the state of charge (SOC) of the batteries (SOC_B) and flywheels (SOC_{FW}), and the control variables as the battery current (I_B) and flywheel torque (T_{FW}):

$$x = \begin{bmatrix} x_1 \\ x_2 \end{bmatrix} = \begin{bmatrix} SOC_B \\ SOC_{FW} \end{bmatrix}, \quad u = \begin{bmatrix} u_1 \\ u_2 \end{bmatrix} = \begin{bmatrix} I_B \\ T_{FW} \end{bmatrix} \tag{6}$$

The SOC of the flywheel is defined in terms of its rotational speed [40], namely $SOC_{FW} = \frac{\omega}{\omega_{max}} \times 100\%$, where ω and ω_{max} are the flywheel speed and maximum speed, respectively, while the SOC of the battery is defined as the electric charge available relative to the maximum capacity, namely $SOC_B = \frac{Q_{battery}}{Q_B} \times 100\%$, where $Q_{battery}$ and Q_B in Ampere-hour are the current and maximum capacity of the battery, respectively. The HESS model is described as follows:

$$\begin{aligned} \dot{x}_1 &= -\tfrac{1}{3600 Q_B} u_1, \\ \dot{x}_2 &= -\tfrac{b}{\omega_{max} J_{FW}} x_2 - \tfrac{1}{\omega_{max} J_{FW}} u_2, \end{aligned} \tag{7}$$

where b and J_{FW} are the drag coefficient and inertia of the flywheel. Note that using battery current and flywheel torque as the control variables allows us to derive a linear model for the B/FW system in the form of (7).

For the B/UC HESS model, we define the states as the state of charge (SOC) of the batteries (SOC_B) and ultra-capacitor (SOC_{UC}), and the control variables as the battery current (I_B) and the ultra-capacitor (I_{UC}):

$$x = \begin{bmatrix} x_1 \\ x_3 \end{bmatrix} = \begin{bmatrix} SOC_B \\ SOC_{UC} \end{bmatrix}, \quad u = \begin{bmatrix} u_1 \\ u_3 \end{bmatrix} = \begin{bmatrix} I_B \\ I_{UC} \end{bmatrix}, \tag{8}$$

where the SOC of the ultra-capacitor is defined as $SOC_{UC} = \frac{V_{UC}}{V_{max}} \times 100\%$, where V_{UC} and V_{max} are the voltage and maximum voltage of ultra-capacitors.

The battery model in B/UC is same as that in B/FW, the ultra-capacitor model is described as follows [20]:

$$\dot{x}_3 = -\frac{1}{V_{max} C_{UC}} u_3, \tag{9}$$

where C_{UC} is the capacitance of the ultra-capacitor.

3. HESS configuration selection and sizing

For this study, we use an electric cargo ship as the example, whose key parameters are shown in Table 1 [20].

To quantitatively compare and analyze the performance of different configurations, three sea states (SS2, SS4 and SS6), corresponding to smooth, moderate and severe operating conditions, respectively, are used in the simulation and analysis. Parameters associated with wave behavior and operating conditions are shown in Table 2.

Table 1
Ship parameters.

Description	Parameter	Value
Ship length	L_{ship}	190 m
Ship breadth	B_{ship}	28.4 m
Draft	H	15.8 m
Mass	m	20,000 ton
Added-mass	m_x	28,755 ton
Thrust deduction coefficient	t_d	0.2
Propeller diameter	D	5.6 m
Wetted area	S	12,297 m^2
Advance facing area in the air	A_T	675.2 m^2
Water resistance coefficients	$C_F + C_R$	0.0043
Air resistance coefficient	C_{air}	0.8

Table 2
Parameters for simulation study.

Description	Parameter	Value
Wave period	T_{wave}	12 sec
Wave height	h_{wave}	0.5 m(SS2)/2 m(SS4)/4 m(SS6)
Wave length	L_{wave}	40.29%L_{ship}
Ship speed command	U_d	12.4 knot
Motor speed command	ω_d	125 rpm

The key technical specifications of the energy storage candidates used for our investigation are:

1. Battery module (BATVXLFP 100 Ah): Flux Power lithium battery module rated at 128 V and 100 Ah storage capacity. The maximum continuous current can be as high as 300 A.
2. Flywheel module (VYCON): Vycon flywheel module rated at maximum charge/discharge power of 90 kW, maximum speed of 36,750 rpm. The motor/generator of the Vycon flywheel is a three-phase permanent magnet machine.
3. Ultra-capacitor module (BMOD0063 P125): Maxwell ultra-capacitor module rated at 125 V, 63 F with maximum charge/discharge current of 240 A.

With the inputs and states defined in Section 2, the terminal powers of battery, flywheel and ultra-capacitor are determined as follows:

$$\begin{aligned} P_B &= N_B \times (V_{OC}(x_1)u_1 - R_B u_1^2), \\ P_{FW} &= N_{FW} \times \left[\omega_{max} x_2 u_2 - \tfrac{3}{2} R_s \left(\frac{u_2}{\frac{3}{4} p_{PM} \Lambda_{FW}} \right)^2 - b(\omega_{max} x_2)^2 \right], \\ P_{UC} &= N_{UC} \times (V_{max} x_3 u_3 - R_{UC} u_3^2), \end{aligned} \tag{10}$$

where N_B, N_{FW} and N_{UC} are the number of battery, flywheel and ultra-capacitor modules, respectively; $V_{OC}(x_1)$ and R_B are the open-circuit voltage and internal resistance of the battery; R_s, p_{PM} and Λ_{FW} are the stator resistance, the number of poles and the permanent magnet flux of the flywheel motor/generator, respectively; R_{UC} is the internal resistance of the ultra-capacitor; and b is the drag coefficient. The parameters of B/FW and B/UC HESS configurations are shown in Table 3. For dynamic applications, as the standby losses of the battery [41] and ultra-capacitor [42] can be ignored, only conduction losses are considered in the battery and ultra-capacitor models. However, the standby loss of the high-speed flywheel, due to the spinning of its rotor, cannot be ignored [43]. The conduction losses of the battery, flywheel and ultra-capacitor are $R_B u_1^2$, $\frac{3}{2} R_s \left(\frac{u_2}{\frac{3}{4} p_{PM} \Lambda_{FW}} \right)^2$ and $R_{UC} u_3^2$, respectively, and $b(\omega_{max} x_2)^2$ is the spinning loss of the flywheel, including windage losses and core losses. We note that the flywheel is operated at its minimum current operation point.

Table 3
B/FW and B/UC hybrid energy storage parameters.

Description	Parameter	Value
Internal resistance of one battery module	R_B	64 mΩ
Maximum speed of one FW module	ω_{max}	36,750 rmp
Stator resistance of one FW module	R_s	6 mΩ
Inertia of one FW module	J_{FW}	0.6546 kg m^2
Capacitance of one UC module	C_{UC}	63 F
Maximum voltage of one UC module	V_{max}	125 V
Internal resistance of one UC module	R_{UC}	8.6 mΩ

Energy conversion by DC/AC inverters and DC/DC converters can introduce additional electrical loss. The efficiency of those power electronic converters highly depends on the hardware (such as power semiconductor devices), topologies and operation conditions [44,45]. The power electronic converters used in hybrid electric vehicles can be modeled in several ways: ideal devices [35], constant conversion factors [46], efficiency lookup tables [34] and physical models (conduction losses and switching losses) [45]. The physical models could provide more accurate information if all the key parameters are available. However, the high-power converters used in shipboard network are not well established. Therefore, the power electronic converters are assumed as ideal devices in this paper. The modeling of those converters with established parameters will be studied in our future work.

Sea state 4 is defined as the nominal sea condition in our design. The HESS sizing in this paper is based on an energy and power requirement analysis of propulsion load fluctuations at sea state 4, shown in Table 4, where the maximum absolute power in one cycle, and energy stored or drawn in one half-cycle, are listed. According to this requirement and the frequency characteristics of the load power, the sizes of the energy storage are selected and shown in Table 5, where the assumed operating conditions are: $I_B = 150$ A, $T_{FW} = 30$ N, $I_{UC} = 240$ A, $SOC_B = 80\%$, $SOC_{FW} = 80\%$, $SOC_{UC} = 80\%$. A sample result of the model response, in both the time domain and frequency domain, is shown in Fig. 1, where the responses in two sea states (sea state 4 and sea state 6) are shown side-by-side. The "Low Frequency" and "High Frequency" in Table 4 represent the low-frequency and high-frequency components, respectively. Since there is no in-and-out-of-water behavior at sea state 4, the low-frequency component is at the encountered wave frequency (around 0.1 Hz) and the high-frequency component is at the propeller-blade frequency (around 8 Hz).

4. Performance evaluation of B/FW and B/UC HESS configurations

In this study, we focus on the feasibility and performance comparison of different HESS configurations, the controls of generators and propulsion motors are not taken into consideration. They are

Table 4
Power and energy requirements at sea state 4.

	Low frequency	High frequency	Total
Maximum power	114 kW	194 kW	308 kW
Energy storage	121 Wh	2.05 Wh	123 Wh

Table 5
HESS configuration and size selection.

	B/FW HESS	B/UC HESS
Battery (N_B)	6 Modules	6 Modules
Flywheel (N_{FW})	3 Modules	0 Modules
Ultra-capacitor (N_{UC})	0 Modules	9 Modules
Maximum power	331 kW	331 kW
Energy storage	69.2 kWh	62.23 kWh

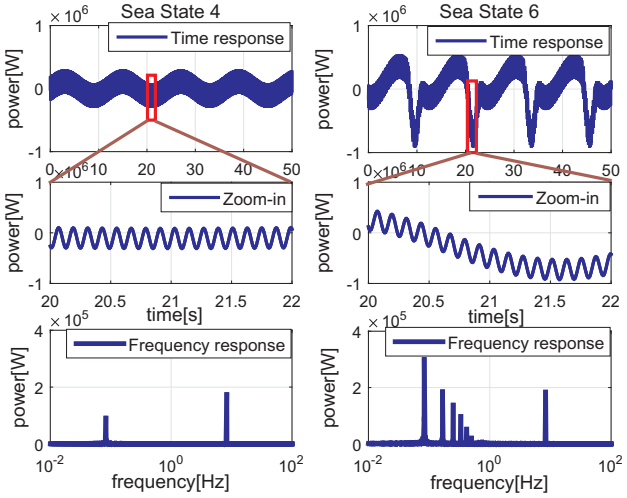

Fig. 1. Load power fluctuations (top plots), zoom-in fluctuations (middle plots), and their frequency spectrums (bottom plots).

assumed to operate at their high-efficiency points and the generators provide the average power for the propulsion system. The energy management strategies of HESS are designed to achieve two objectives: one is to minimize the power tracking error, measured by the root mean square (RMS) error for mitigating load fluctuations and buffering generator sets, and the other is to reduce HESS losses to improve energy efficiency:

$$J_1 = \sum_{k=0}^{N_T} (P_{FL}(k) - P_{HESS}(k))^2, \tag{11}$$

$$J_2 = \sum_{k=0}^{N_T} (P_{HESS_{Loss}}), \tag{12}$$

where $N_T = [(t_T - t_0)/T_s]$, with $[\cdot]$ being the integer rounding of $\cdot$, t_0 and t_T are the initial and final values of the time period being investigated, T_s is the sampling time, P_{FL} is the load power fluctuation from the propeller and ship dynamics model, P_{HESS} is the power generated by HESS to compensate the load fluctuations, and $P_{HESS_{Loss}}$ is the HESS losses. Note that the RMS tracking error can be expressed as $\sqrt{J_1/N_T}$. Since N_T is constant, minimizing J_1 is equivalent to minimizing the RMS tracking error.

Because J_1 and J_2 compete in the sense that reducing the tracking error would cause increased HESS losses, and vice versa, the weighted-sum method, which converts the multi-objective optimization problem (MOP) to a single-objective optimization problem, is used to find the non-dominated solutions (i.e., Pareto-front) in this problem. The problem formulation of B/FW is expressed as follows. Minimize:

$$\begin{aligned} J_{HESS_{B/FW}}(x(k),u(k)) = \sum_{k=0}^{N_T} & (1-\lambda)(P_{FL}(k) - P_B(k) - P_{FW}(k))^2 \\ & + \lambda \left[N_B R_B u_1^2(k) + N_{FW}(b(\omega_{max} x_2(k))^2 \right. \\ & \left. + \frac{3}{2} R_s \left(\frac{u_2(k)}{\frac{3}{4} p_{PM} \Lambda_{FW}} \right)^2) \right], \end{aligned} \tag{13}$$

subject to the constraints:

$$\begin{aligned} & 20\% \leqslant x_1 \leqslant 90\%, \\ & 30\% \leqslant x_2 \leqslant 99\%, \\ & -200 \text{ A} \leqslant u_1 \leqslant 200 \text{ A}, \\ & -40 \text{ N m} \leqslant u_2 \leqslant 40 \text{ N m}, \\ & -90 \text{ kW} \leqslant u_2 x_2 \omega_{max} \leqslant 90 \text{ kW}, \end{aligned} \tag{14}$$

$$\begin{bmatrix} x_1(k+1) \\ x_2(k+1) \end{bmatrix} = \begin{bmatrix} 1 & 0 \\ 0 & 1-\frac{bT_s}{\omega_{max} J_{FW}} \end{bmatrix} \begin{bmatrix} x_1(k) \\ x_2(k) \end{bmatrix} + \begin{bmatrix} \frac{T_s}{3600 Q_B} & 0 \\ 0 & \frac{T_s}{\omega_{max} J_{FW}} \end{bmatrix} \begin{bmatrix} u_1(k) \\ u_2(k) \end{bmatrix}, \tag{15}$$

while the problem formulation for the B/UC HESS is given by:

$$J_{HESS_{B/UC}}(x(k),u(k)) = \sum_{k=0}^{N_T} (1-\lambda)(P_{FL}(k)-P_B(k)-P_{UC}(k))^2 + \lambda (N_B R_B u_1^2(k) + N_{UC} R_{UC} u_3^2(k)), \tag{16}$$

subject to the constraints:

$$\begin{aligned} &20\% \leqslant x_1 \leqslant 90\%, \\ &30\% \leqslant x_3 \leqslant 99\%, \\ &-200 \text{ A} \leqslant u_1 \leqslant 200 \text{ A}, \\ &-240 \text{ A} \leqslant u_3 \leqslant 240 \text{ A}, \end{aligned} \tag{17}$$

$$\begin{bmatrix} x_1(k+1) \\ x_3(k+1) \end{bmatrix} = \begin{bmatrix} 1 & 0 \\ 0 & 1 \end{bmatrix} \begin{bmatrix} x_1(k) \\ x_3(k) \end{bmatrix} + \begin{bmatrix} \frac{T_s}{3600 Q_B} & 0 \\ 0 & \frac{T_s}{V_{max} C_{UC}} \end{bmatrix} \begin{bmatrix} u_1(k) \\ u_3(k) \end{bmatrix}, \tag{18}$$

where $\lambda \in [0,1]$ is a weighting factor that allows us to put different relative emphasis on each attribute to investigate the performance trade-off.

In order to evaluate the feasibility and effectiveness of the B/FW HESS, we perform a comparative study to determine the advantages and disadvantages of B/FW and B/UC HESS configurations. In this case study, the sampling time for the control update is chosen as 0.02 s, which is properly matched with the underlying system dynamics. We define the time interval that the HESS can be used as the energy buffer for the electric propulsion system without requiring charging or discharging from external power sources (such as the diesel generator) as the self-sustained operation period. A longer self-sustained operation could offer more flexible charging or discharging for the HESS, therefore leading to better efficiency. The self-sustained operation time is chosen to be 30 min, over which the resulting performance is evaluated in terms of the following two metrics that are closely related to the aforementioned objectives:

1. RMS tracking error: $\sqrt{J_1/N_T}$.
2. HESS losses: $Loss\% = \frac{J_2}{\sum_{k=0}^{N_T} P_{FL}(k)} \times 100\%$.

The weighting factor λ allows us to put a different relative emphasis on each attribute to investigate the performance trade-off. The global optimal solutions of B/FW and B/UC MOPs are obtained by dynamic programming (DP). DP is widely used to obtain global optimal solutions and provide the guideline for real-time control development [34,47]. Typically, standard DP can be divided into 3 steps:

1. Quantize state and control values as well as instantaneous cost (transitional cost) $L(x,u,k)$ for $k = 1,2...N_T$ into finite grids.
2. Solve recursive equation backwards to obtain "cost to go" function $J^*(x,k) = \min\{L(x,u,k) + J^*(f(x,u,k),k+1)\}$ and the optimal control policy $u^*(x,k) = \text{argmin}\{L(x,u,k) + J^*(f(x,u,k),k+1)\}$ for $k = N_T, N_T-1...,1$.
3. Retrieve the optimal solution forward for a given initial state: $x(k+1) = f(x,u^*(x,k),k)$ for $k = 1,2...N_T$.

The instantaneous cost $L(x,u,k)$ in the first step requires more computational time and hardware memory, compared with others. Note that parallel interpolations can be used to increase the computational efficiency in the second step. To reduce the required hardware memory and computational time, the periodic characteristic of shipboard propulsion-load fluctuations is taken into consideration in this paper. The period of the encountered wave is defined as T_P. The propulsion-load fluctuations under periodic steady state can be expressed as:

$$P_{FL}(t+T_P) = P_{FL}(t) \tag{19}$$

Then the instantaneous cost in the first step can be also expressed as $L(x,u,t+T_P) = L(x,u,t)$.

According to this periodic characteristic, a periodic DP is developed. The number of the wave period within the investigation time is defined as n_P and the time steps of one period is defined as N_P. Note that N_T can be expressed by n_P and N_P: $N_T = n_P N_P$. The comparison between the standard DP and periodic DP is shown in Fig. 2. In the first step, only one period information are required to be computed and recorded. When the investigation time consists of considerable periods, the required hardware memory and computational time can be significantly reduced. In this study, the number of the wave period is $n_P = 150$. The computational time and required memory in the standard DP are over 100 times larger than the proposed periodic DP.

	Standard DP	Periodic DP
Step 1	$k = 1,2,...,n_p N_p$ $L(x,u,k) \quad x(k+1) = f(x,u,k)$	$k = 1,2,...,N_p$ $L(x,u,k) \quad x(k+1) = f(x,u,k)$
Step 2	$k = n_F T_F, n_F T_p - 1,...,1$ $J^*(x,k) = \min_{u \in U}\{L(x,u,k) + J^*(f(x,u,k),k+1)\}$ $u^*(x,k) = \arg\min_{u \in U}\{L(x,u,k) + J^*(f(x,u,k),k+1)\}$	$m = n_p - 1, n_p - 2,...,0$ $i = N_p, N_p - 1,...,1$ $k = mN_p + i$ $J^*(x,k) = \min_{u \in U}\{L(x,u,i) + J^*(f(x,u,i),k+1)\}$ $u^*(x,k) = \arg\min_{u \in U}\{L(x,u,i) + J^*(f(x,u,i),k+1)\}$
Step 3	$k = 1,2,...,n_p N_p \quad x(1) = x_0$ $x(k+1) = f(x,u^*(x,k),k)$	$k = 1,2,...,n_p N_p \quad x(1) = x_0$ $x(k+1) = f(x,u^*(x,k),k)$

Fig. 2. Dynamic programming comparison: standard DP vs. periodic DP.

The Pareto-fronts of these two configurations, which represent the best achievable performance for the system with B/FW HESS and B/UC HESS, are shown in Figs. 3–5. The Pareto fronts provide insight into the effectiveness of HESS and the trade-off between the tracking RMS error and the HESS losses. The key observations are summarized in the following remarks:

Remark 4.1 (*Performance trade-off features*). Over a wide range, the tracking performance can be improved at little cost of system efficiency for low and medium sea states (sea states 2 and 4). This feature can be observed for both B/FW and B/UC HESS solutions. Furthermore, the general trends and Pareto front shapes are the same for both HESS configurations at all sea states. In terms of managing the trade-off, they both have the same features and issues.

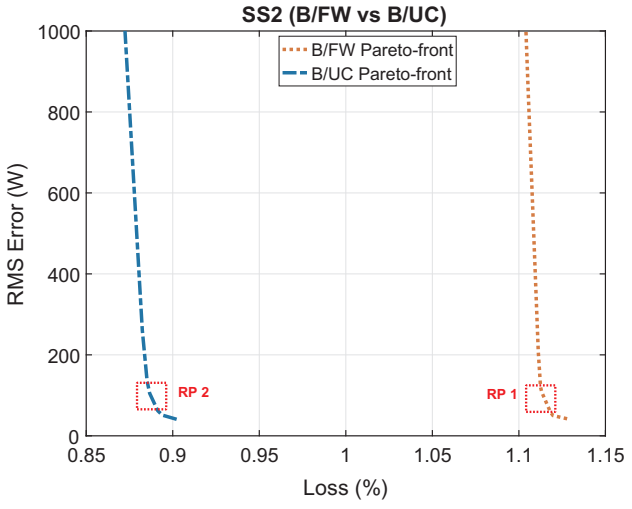

Fig. 3. Pareto-fronts of B/FW and B/UC HESS at sea state 2.

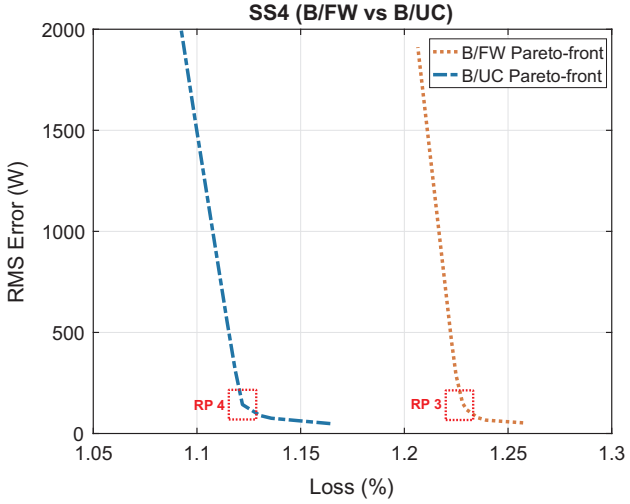

Fig. 4. Pareto-fronts of B/FW and B/UC HESS at sea state 4.

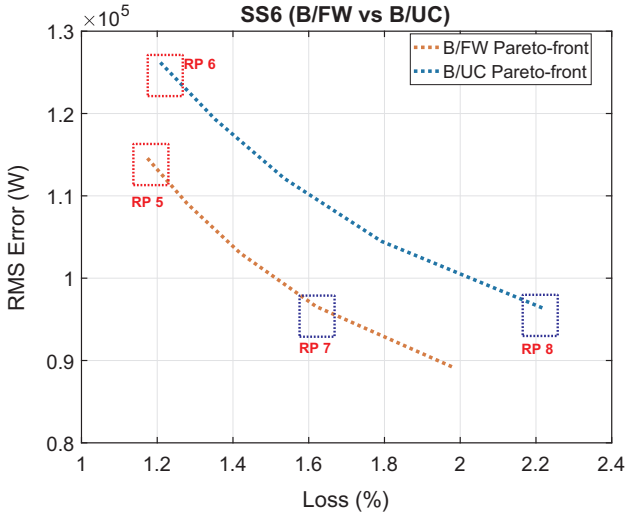

Fig. 5. Pareto-fronts of B/FW and B/UC HESS at sea state 6.

Remark 4.2 (*B/FW vs. B/UC*). As shown in Figs. 3–5, the B/FW HESS is able to achieve superior performance at sea state 6. However, at sea states 2 and 4, the B/UC HESS achieves better performance than B/FW HESS, but the difference between B/FW HESS losses and B/UC HESS losses at sea state 2 (around 0.22%) is about twice as large as that at sea state 4 (around 0.11%). Note that the load power fluctuations at sea state 2 are smaller than those at sea state 4. The analysis indicates that B/FW HESS is more suitable for the high sea state, while the B/UC HESS has performance advantages at low sea states.

To reveal more details of the HESS performance, several representative points (RP) are highlighted in Figs. 3–5 for further analysis. As shown in Figs. 3 and 4, those points reflect the best trade-off between two objectives and they are closest to the "utopia" points (J_{1min},J_{2min}). Therefore, RP1–RP4 are the design points analyzed here. The RMS tracking errors of these design points, i.e., RP1–RP4, are almost the same at the same sea state. RP5–RP8 are the points with comparable performance in one of the attributes at sea state 6. Besides the two main objectives in Figs. 3–5, several other metrics are used for evaluating these solutions as shown in Table 6:

The $I_{B_{RMS}}$, $I_{B_{Peak}}$ and $I_{B_{1.5C}}\%$ are used to evaluate the battery usage as they have high impact on the battery life; power losses of each energy storage as well as the losses due to different mechanism in the flywheel provide insight into the operation of HESS. The key observations about the reference points are summarized in the following remarks:

Table 6
Performance metrics.

$I_{B_{RMS}}$	Battery currents measured by the rms (root mean square) value
$I_{B_{Peak}}$	Battery currents measured by the maximum absolute value
$T_{I_{B_{1.5C}}}\%$	The time spent charging/discharging the battery with high currents: the percentage of high current operation ($\|I_B\| \geqslant 1.5C$)
$Loss_B\%$	Battery conduction loss: $Loss_B\% = \frac{\sum_{k=0}^{N_T}(Power_{B-loss}(k))}{\sum_{k=0}^{N_T} P_{Demand}(k)} \times 100\%$
$Loss_{UC}\%$	Ultra-capacitor conduction loss: $Loss_{UC}\% = \frac{\sum_{k=0}^{N_T}(Power_{UC-loss}(k))}{\sum_{k=0}^{N_T} P_{Demand}(k)} \times 100\%$
$Loss_{FW_{Rs}}\%$	Flywheel conduction loss: $Loss_{FW_{Rs}}\% = \frac{\sum_{k=0}^{N_T}(Power_{FW_{Rs}-loss}(k))}{\sum_{k=0}^{N_T} P_{Demand}(k)} \times 100\%$
$Loss_{FW_f}\%$	Flywheel spinning loss: $Loss_{FW_f}\% = \frac{\sum_{k=0}^{N_T}(Power_{FW_f-loss}(k))}{\sum_{k=0}^{N_T} P_{Demand}(k)} \times 100\%$

Remark 4.3 (*Battery usage*). B/FW HESS is more 'friendly' to batteries with smaller $I_{B_{RMS}}$,$I_{B_{Peak}}$, and less time spent at high-current operation $T_{I_{B_{1.5C}}}\%$, as shown in Table 7. At sea state 2, $I_{B_{RMS}}$ and $I_{B_{Peak}}$ of B/UC HESS are almost twice as large as those of B/FW HESS. At sea state 4, the B/FW HESS requires less $I_{B_{RMS}}$ and $I_{B_{Peak}}$ than B/UC to achieve almost the same tracking error. At sea state 6, RP5 and RP6 have almost the same HESS losses, but RP5 (B/FW) achieves much smaller power tracking RMS error. B/FW HESS requires less battery usage and high-current operation, while achieving improved power tracking performance. For RP7 and RP8, the battery high-current operation for B/UC HESS is even more than twice of that for B/FW.

Remark 4.4 (*Loss analysis*). At sea state 2, even though both the battery RMS and peak current with B/FW are less than those with B/UC, the loss of B/FW is larger than that of B/UC. The reason for this is that the standby loss of the flywheel, namely the spinning loss, is significant at the low sea state. In particular, the battery needs to discharge more to compensate the spinning losses of the flywheel in order to keep the flywheel working at its optimal speed. Therefore, the drag coefficient is the key design parameter of the flywheel, especially for a high-speed flywheel. At high sea state, the spinning loss of the flywheel is not the main issue of the B/FW HESS configuration. The high power demand of the low-frequency load fluctuation requires the HESS to provide or absorb the maximum power for several seconds. The flywheel working in its high speed range sustains for a longer period of time to generate or absorb the maximum power when compared to the ultra-capacitor. Therefore, as shown in Table 7 and Fig. 5, B/FW can outperform B/UC in terms of improved tracking performance, reduced HESS losses, and extended battery life cycle. Note that some flywheel designs can have lower spinning loss (e.g., synchronous reluctance machines), but they have lower power density and full-load efficiency.

Remark 4.5 (*Sensitivity to battery aging*). It has been widely reported that batteries degrade over their life cycle, as the battery capacity will decrease and the battery resistance will increase [48]. A sensitivity study is performed to provide insights into the impact of the battery state of health (SOH) on the proposed HESS solutions. In this study, SOH is characterized by the capacity reduction and resistance increase percentage. As shown in Fig. 6, the increased resistance has a more significant impact on the proposed solutions, compared to the decreased capacity. The HESS works as an energy buffer instead of an energy source, because the generator sets provide the average power for

Table 7
Performance comparison of the selected design points.

	RP1	RP2	RP3	RP4	RP5	RP6	RP7	RP8
Sea state	2	2	4	4	6	6	6	6
$I_{B_{RMS}}$	12.13A	17.33A	16.02A	21.51A	51.59A	55.86A	74.96A	95.62A
$I_{B_{Peak}}$	31.48A	52.85A	72.00A	82.00A	200A	200A	200A	200A
$T_{I_{B_{1.5C}}}$%	0	0	0	0	3.67%	4%	8.50%	19.0%
$Loss_B$%	0.05%	0.09%	0.07%	0.13%	0.39%	0.46%	0.82%	1.34%
$Loss_{UC}$%	NA	0.80%	NA	0.99%	NA	0.75%	NA	0.88%
$Loss_{FWR_S}$%	0.53%	NA	0.48%	NA	0.35%	NA	0.36%	NA
$Loss_{FW_f}$%	0.54%	NA	0.67%	NA	0.43%	NA	0.44%	NA

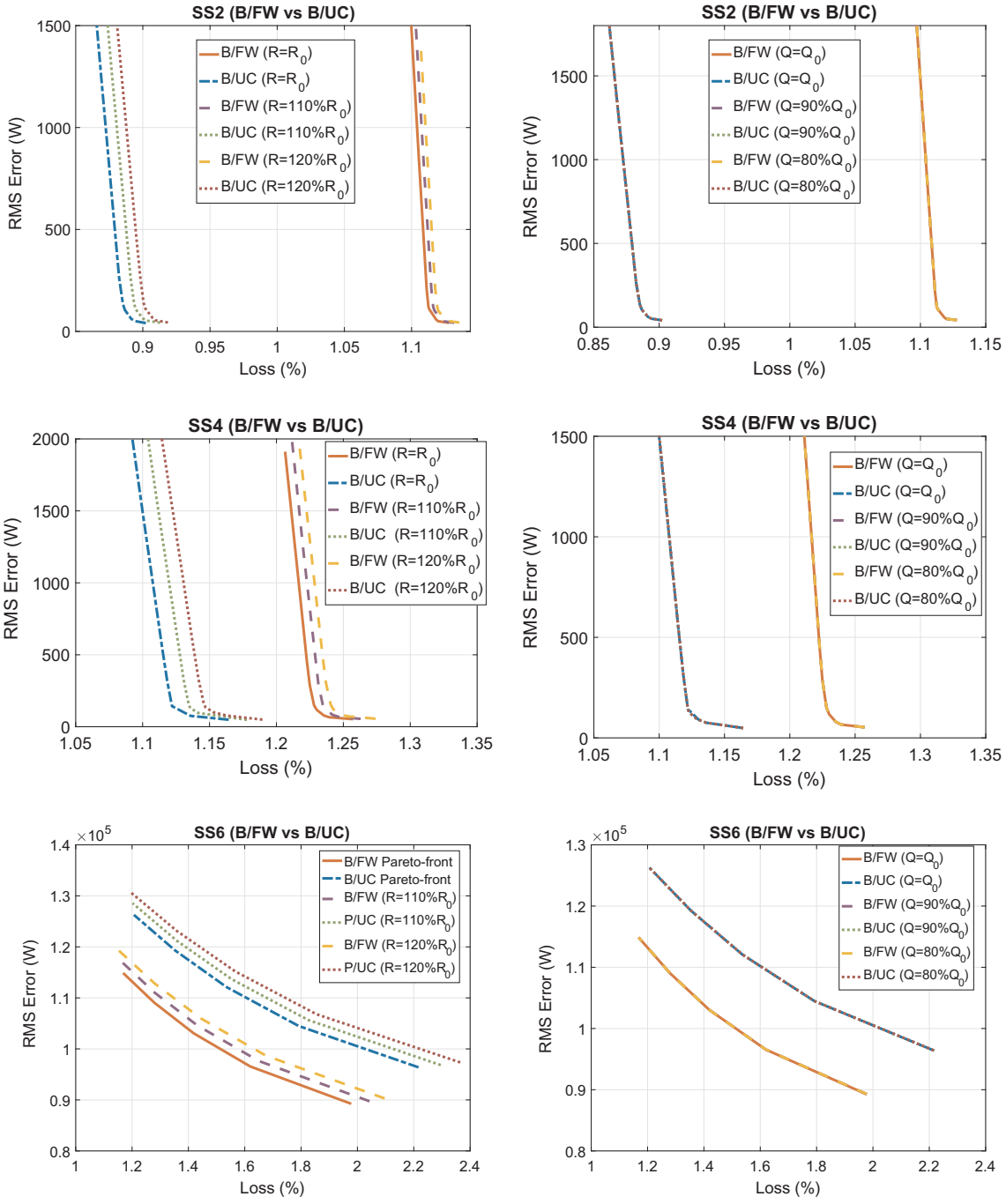

Fig. 6. Pareto-fronts of B/FW and B/UC HESS at sea states 2, 4 and 6 with different battery state of health.

the electric propulsion system. Due to the high energy density of the battery, the battery SOC variation within the self-sustained time is very small. Although the degraded capacity can increase the SOC variation, the battery open circuit voltage $V_{OC}(x_1)$ is in general insensitive to this small SOC variation. Therefore, the impact of the decreased capacity is relatively small. The impact of the increased resistance on the B/UC HESS at sea states 2 and 4 is larger than it is on the B/FW HESS. As discussed in the previous remarks, the spinning losses of the flywheel is dominant in B/FW HESS at low sea state, as shown in Table 7, whereas the battery resistance, which affects the battery loss, has less effect. However, at high sea state, due to the high-power fluctuations, the battery losses become more significant even in the B/FW configuration. Therefore, the sensitivity to battery resistance is noticeable for both B/FW and B/UC HESS.

The MOP formulated here can be used to evaluate the effectiveness of different HESS configurations and analyze their advantages and limitations. However, the solution of the MOP cannot be used for real-time applications. It is an open-loop optimization without feedback. Furthermore, this optimization problem has a very long horizon in the sense that 90,000 steps are involved when the minimum self-sustained operation time of HESS is chosen to be 30 min. This requires a long computational time and large memory, which makes it computationally prohibitive to solve in real time, and leads to the MPC formulation discussed in the next section.

5. Energy management with HESS

In this section, the receding-horizon approach is applied to develop a real-time energy management scheme. To capture the dynamics of HESS and address the associated operation constraints, MPC emerges as a natural choice [49,50]. The general MPC problem, which minimizes a cost function subject to constraints within the predictive horizon, can be mathematically expressed as:

$$J = \Phi(x(t+N)) + \sum_{k=t}^{t+N-1} L(x(k),u(k)), \tag{20}$$

subject to:

$$x(k+1) = f(x(k),u(k)), \quad x(t) = x_0, \tag{21}$$

$$C(x(k),u(k)) \leqslant 0, \tag{22}$$

where $\Phi(x(t+N))$ and $L(x(k),u(k))$ are the terminal and instantaneous cost functions, N is the time window over which the cost will be evaluated, $x(k)$ and $u(k)$ are the instantaneous values of the states ($x \in \Re^2$) and controls ($u \in \Re^2$) at time k, respectively, $C(x(k),u(k))$ represents the inequality constraints, and t represents the current sample time. By minimizing (20) subject to (21) and (22), an optimized control sequence $u^*(t),u^*(t+1),...,u^*(t+N-1)$ can be obtained. The standard receding horizon MPC then applies the first element of the sequence as the control action before moving to the next sample, when new measurements are collected and the optimization is repeated with new initial conditions [51–53].

The cost function in MPC is formulated based on the MOP by using the weighted-sum method. We discretize the system model developed in Section 2 with sampling time T_s. No terminal cost is incorporated in this MPC formulation. Therefore, the MPC formulation of B/FW is defined as:

$$J_{HESS_{B/FW}} = \sum_{k=t}^{t+N-1} L_{HESS_{B/FW}}(x(k),u(k)), \tag{23}$$

where

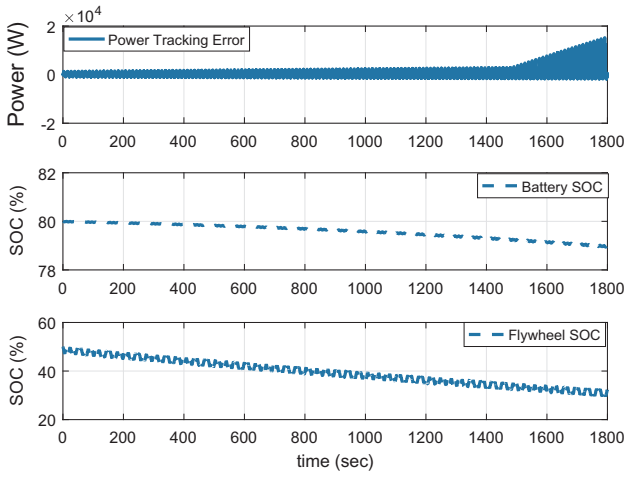

Fig. 7. B/FW HESS performance at sea state 4 without any penalty on the speed of FW.

$$L_{HESS_{B/FW}}(x(k),u(k)) = (1-\lambda)(P_{FL}(k)-P_B(k)-P_{FW}(k))^2 + \lambda\left[N_B R_B u_1^2(k) + N_{FW}\left(b(\omega_{max}x_2(k))^2 + \frac{3}{2}R_s\left(\frac{u_2(k)}{\frac{3}{4}p_{PM}\Lambda_{FW}}\right)^2\right)\right], \tag{24}$$

subject to the constraints (14) and (15), where $\lambda \in [0,1]$ is the weighting factor that allows us to put different relative emphasis on each attribute to investigate the performance trade-off.

The short-horizon MPC, however, cannot incorporate the long-term aspects of operation. As a result, we observed that the SOC of the flywheel drops quickly. As it decreases, delivering the same output power requires larger torque, thereby leading to significantly increased losses and power tracking error, as shown in Fig. 7.

To keep the flywheel working in a high-efficiency range without having to extend the MPC predictive horizon, we analyzed the DP results to help us find mechanisms to assure long-term system efficiency. The representative point RP3 as shown in Fig. 4 is used as a benchmark in this section. As shown in Fig. 8, the B/FW HESS operation can be divided into three phases: transient, steady-state, and final. Given different initial SOCs of the flywheel, it converges to the same SOC range, which is the high-efficiency range for B/FW HESS, during the transient.

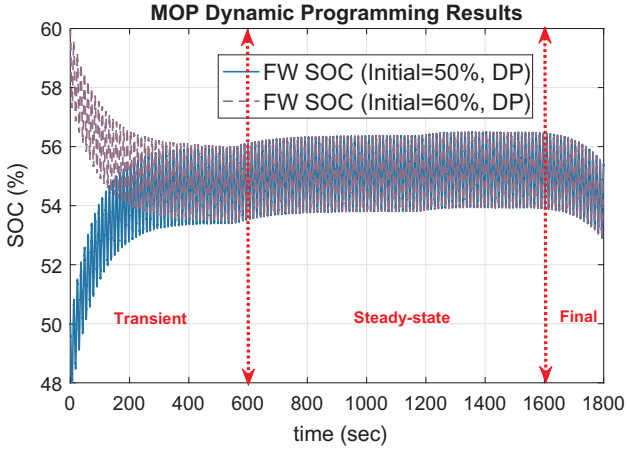

Fig. 8. The flywheel SOC of MOP dynamic programming solutions with different initial SOCs.

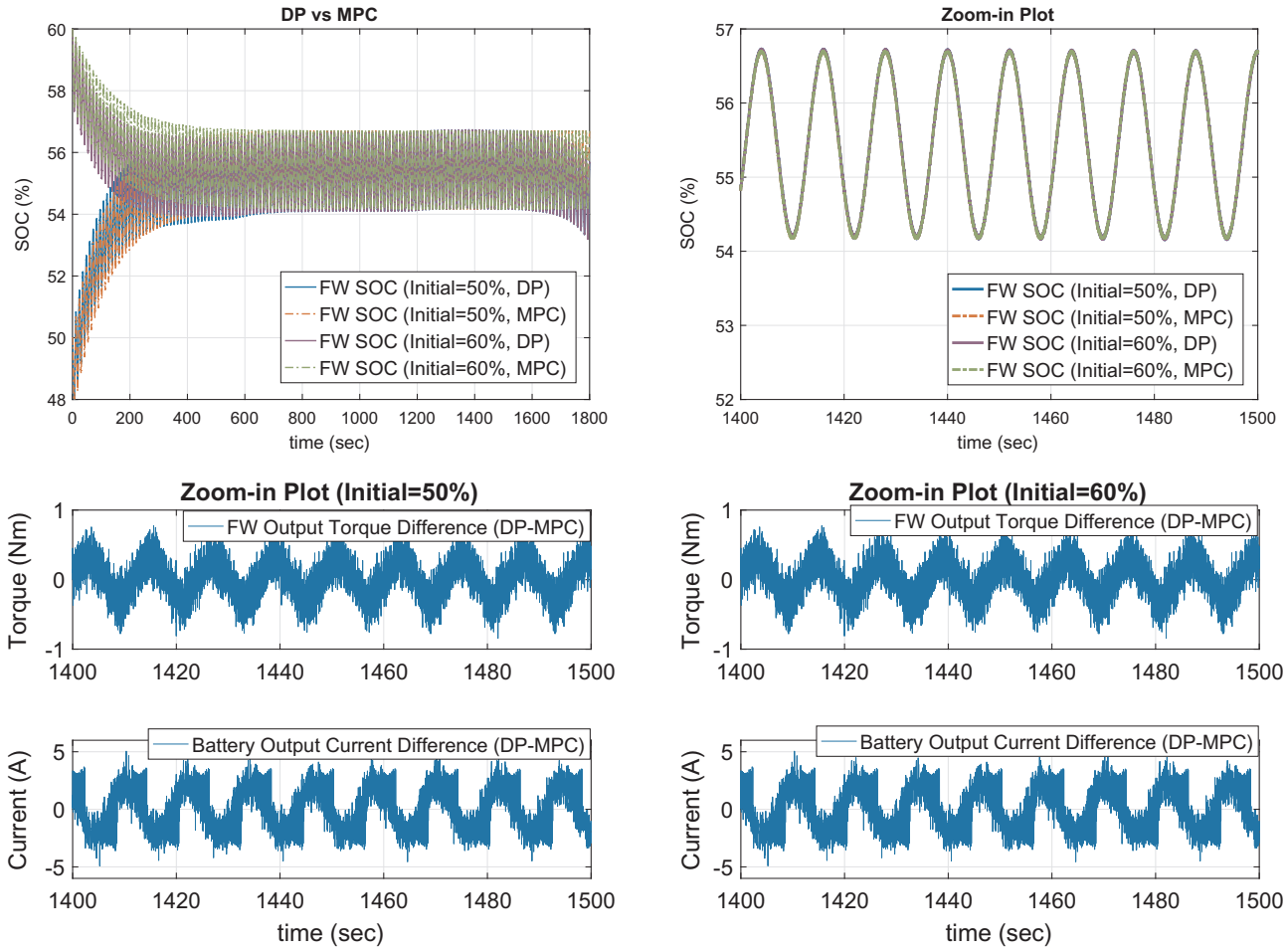

Fig. 9. The performance comparison: MPC vs. DP.

When the B/FW HESS is operating at steady-state, the battery will keep the flywheel SOC in its high-efficiency range to minimize the cost in (13). At the final phase, the battery is not required to maintain the flywheel SOC, then the flywheel will be used as much as possible. In order to maximize the benefits of B/FW HESS, a long self-sustained time is preferred. For a long self-sustained time, steady-state operation is the key, which requires that the flywheel works in its high-efficiency SOC range. This observation motivates us to add another term to the cost function with a penalty on the SOC deviations from the optimal settings is introduced in (13):

$$\gamma_{FW_{SOC}}\left(x_2(k)-SOC_{FW_d}\right)^2, \tag{25}$$

The cost function used in the MPC optimization formulation then has the form:

$$\begin{aligned} L_{HESS_{B/FW}}(x(k),u(k)) = {} & (1-\lambda)(P_{FL}(k)-P_B(k)-P_{FW}(k))^2 \\ & + \lambda\left[N_B R_B u_1^2(k)\right. \\ & \left. + N_{FW}\left(b(\omega_{max}x_2(k))^2 + \frac{3}{2}R_s\left(\frac{u_2(k)}{\frac{3}{4}p_{PM}\Lambda_{FW}}\right)^2\right)\right] \\ & + \gamma_{FW_{SOC}}\left(x_2(k)-SOC_{FW_d}\right)^2; \end{aligned} \tag{26}$$

Increasing γ initially improves the performance, but further increase in γ beyond a certain value will lead to deteriorated performance. The reason is that, when initially increasing γ, the flywheel can operate around its optimal SOC, leading to improved efficiency. However, if γ is too large, then the flywheel is forced to operate close to its optimal SOC with small variations, which leaves most of the compensation function on the batteries. That makes the HESS function essentially a battery energy storage system, thereby losing the advantage of the hybrid configuration. By varying γ, we are able to obtain the best achievable solution. In this study, γ is tuned off-line. Note that how to obtain the optimal reference SOC is an open question and will be explored in future work. This paper focuses on the investigation of the B/FW HESS feasibility and effectiveness.

The performance of the proposed MPC energy management strategy and DP is shown in Fig. 9. As shown in the zoom-in plots of Fig. 9, the flywheel SOC under the proposed MPC can achieve the same trajectory as DP at steady-state. The battery output current and flywheel output torque of MPC and DP are also almost the same, thereby achieving almost equivalent performance. The performance metrics in Table 6 and the two main objectives, i.e., RMS tracking error "RMS Error" and HESS losses "*Loss%*", are used to evaluate the steady state performance of the proposed MPC and DP with different initial flywheel SOC. The first group is defined as "DP (50%) and MPC (50%)", i.e., the initial SOC of the B/FW HESS is $x_1(t) = 80\%$, $x_2(t) = 50\%$, and the second one is defined as "DP (60%) and MPC (60%)", i.e., the initial SOC of the B/FW HESS is $x_1(t) = 80\%$, $x_2(t) = 60\%$. For different initial SOCs, the γ is fixed. The best performance metrics are in blue, and the worst are in red. As shown in Table 8, the performance of MPC is close to that of DP. The DP global optimal solution achieves better performance in terms of two main objectives in the cost function, i.e., "*Loss%*" and "RMS Error". MPC achieves smaller peak current ($I_{B_{Peak}}$) and less battery usage ($I_{B_{RMS}}$), leading to less battery losses and extended battery life. Note that the differences between MPC and DP are relatively small. This case

Table 8
Performance comparison of the proposed MPC and DP.

	DP (50%)%	MPC (50%)	DP (60%)	MPC (60%)
$I_{B_{RMS}}$	16.75A	16.25A	15.57A	14.81A
$I_{B_{Peak}}$	101A	101A	66.48A	60.4A
$I_{B_{1.5C}}$%	0	0	0	0
$Loss_B$%	0.08%	0.08%	0.07%	0.06%
$Loss_{FWR_s}$%	0.48%	0.49%	0.48%	0.48%
$Loss_{FW_f}$%	0.67%	0.67%	0.67%	0.69%
Loss%	1.23%	1.24%	1.22%	1.23%
RMS error	153.39 W	197.54 W	148.57 W	179.63 W

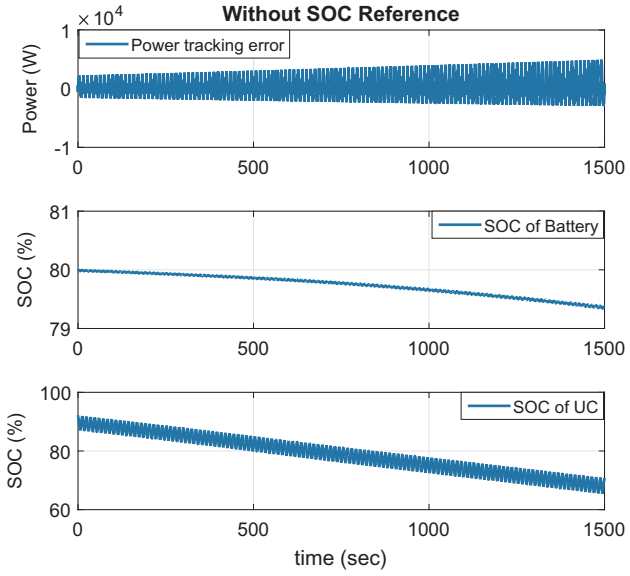

Fig. 10. MPC (N = 20, without UC SOC penalty) performance at sea state 4.

study demonstrates the effectiveness of the proposed MPC in terms of power-fluctuation compensation, HESS energy saving, and reduction of the battery usage, in particular high-current operation.

The proposed MPC can be easily and effectively extended to the B/UC HESS solution. As shown in Fig. 10, without the SOC penalty of UC, the short-horizon MPC is not able to maintain the UC operating in its high SOC range. As a result, the SOC of the UC drops quickly. As it decreases, the delivery of the same output power requires a larger current, thereby leading to significantly increased losses and power tracking error.

Therefore, to keep the UC working in a high efficiency range, another penalty on the UC SOC is considered for B/UC HESS:

$$\gamma_{UC_{SOC}}\left(x_3(k)-SOC_{UC_d}\right)^2, \tag{27}$$

The effectiveness of this $\gamma_{UC_{SOC}}$ penalty is demonstrated by Fig. 11.

In order to validate the proposed MPC approach, a laboratory-scaled experiment is performed in a physical test-bed. The test-bed photo is shown in Fig. 12. Although the proposed MPC significantly reduces the requirement of a long predictive horizon, solving this nonlinear optimization problem is still a challenge for real-time applications. Therefore, the goal of this experiment is to demonstrate the real-time feasibility of the proposed MPC and validate its control performance. In this experiment, the resistive load is used to generate the load fluctuations, which are scaled to a peak value of 3.5 kW. The B/UC HESS is used to

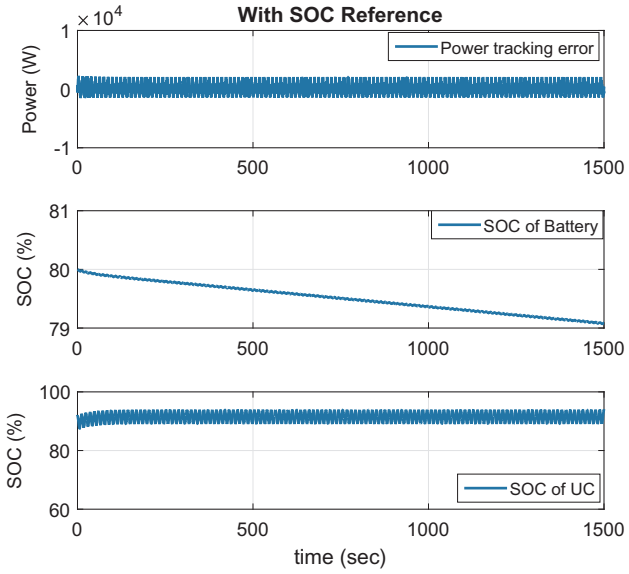

Fig. 11. MPC (N = 20, with UC SOC penalty) performance at sea state 4.

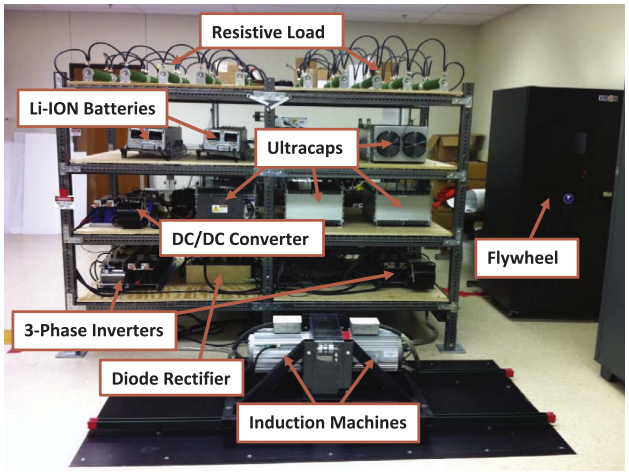

Fig. 12. Laboratory-scaled test-bed with hybrid energy storage devices.

compensate the load fluctuations and maintain a stable DC bus voltage. The desired DC bus voltage is defined as 200 V. The maximum voltage and the desired reference voltage of UC are defined as 140 V and 137 V, respectively. The maximum and minimum output currents of the battery and UC are 30 A and −30 A, respectively. Note that the proposed MPC is used for energy management, namely power split. An additional voltage regulator is used to deal with disturbances and uncertainties. Uncertainties, such as load uncertainties, parameter uncertainties, modeling uncertainties, and measurement uncertainties, exist in the system and can be used to evaluate the robustness of the proposed controller.

The effectiveness of the proposed MPC is validated, as shown in Fig. 13, where the load fluctuations with high and low frequency components are generated by the resistive load bank. The HESS is able to compensate load fluctuations and maintain the DC bus voltage at 200 V. The UC is operating around its reference SOC, namely 137 V. This experiment also demonstrates the real-time feasibility of the proposed MPC for real-time applications.

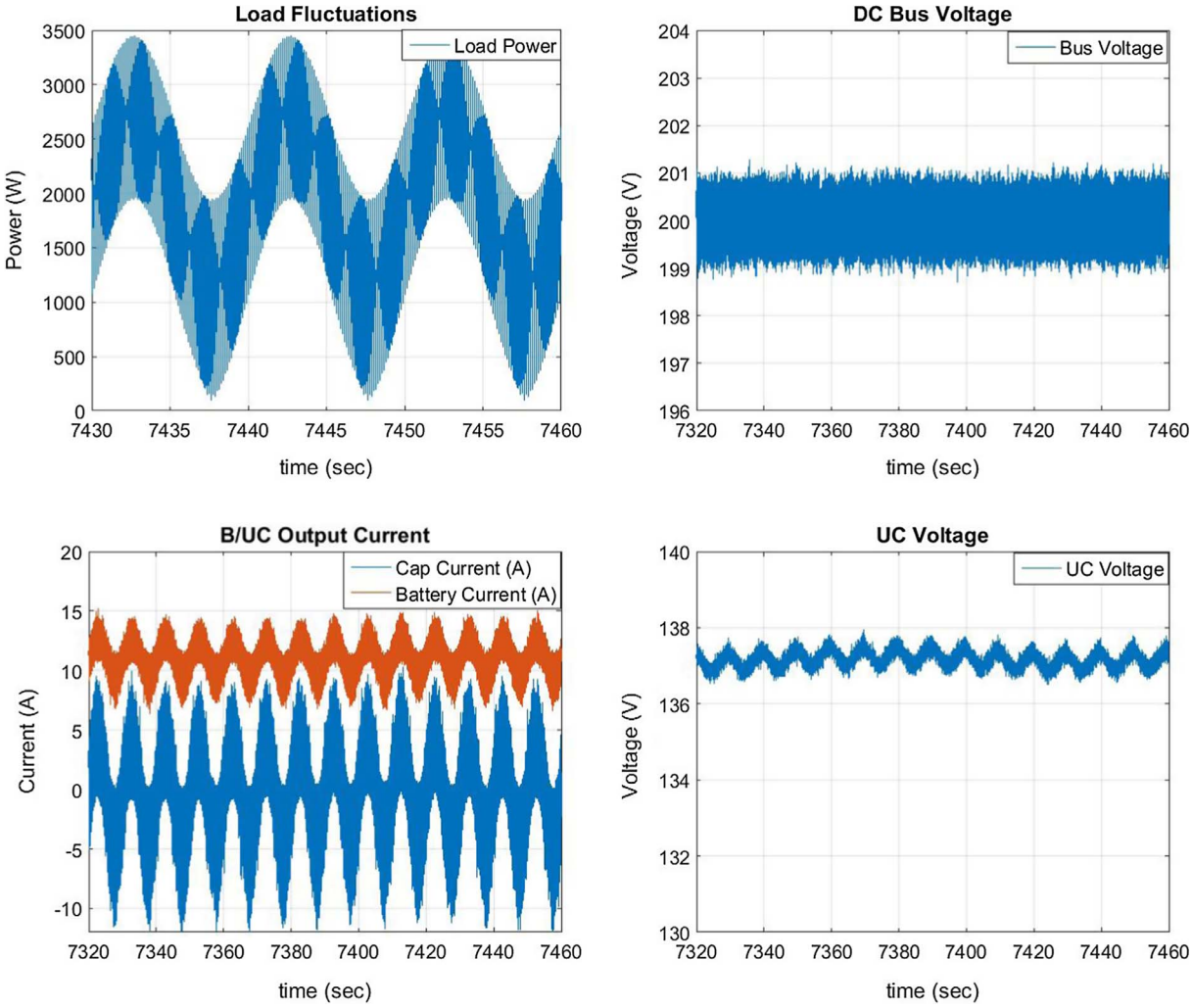

Fig. 13. Experimental validation of B/UC HESS: load fluctuations, DC bus voltage, HESS output currents and UC voltage.

6. Conclusions

This paper investigates the feasibility and effectiveness of a new hybrid energy storage system configuration, namely batteries combined with flywheels, to mitigate load fluctuations, and performs a comparative study with the battery and ultra-capacitor combined configuration. A multi-objective optimization problem (MOP) is formulated to minimize the power tracking error and HESS losses. The best achievable solutions, namely Pareto fronts, are obtained by using dynamic programming. The comparison results indicate that the B/FW HESS configuration outperforms B/UC HESS at high sea state in terms of power fluctuation compensation and HESS efficiency. However, the spinning loss of the B/FW HESS configuration will cause more losses at low sea state, which makes B/UC HESS configuration more suitable in these conditions. Furthermore, B/FW HESS is more “friendly” to batteries in terms of less battery usage, reduced peak current, and less high-current operation for batteries. In order to enable the real-time implementation, a model predictive control algorithm is formulated to minimize the tracking RMS error and HESS losses. In order to overcome the limitations caused by the short predictive horizon of MPC, an additional penalty on the SOC is introduced to keep the HESS working in the high-efficiency operation range. The comparison results of MPC and MOP demonstrate the effectiveness of the proposed MPC in terms of power-fluctuation compensation, HESS energy saving, and reduction of the battery usage and high-current operation. A laboratory-scaled experiment is performed to validate the proposed approach for the real applications.

References

[1] Doerry N. Naval power systems: integrated power systems for the continuity of the electrical power supply. IEEE Electrific Magaz 2015;3(2):12–21.
[2] Doerry N, McCoy K. Next generation integrated power system: NGIPS technology development roadmap, DTIC Document. Tech. Rep.; 2007.
[3] McCoy TJ. Electric ships past, present, and future. IEEE Electrific Magaz 2015;3(2):4–11.
[4] Doerry N, Amy J, Krolick C. History and the status of electric ship propulsion, integrated power systems, and future trends in the us navy. Proc IEEE 2015;103(12):2243-51.
[5] Zahedi B, Norum LE, Ludvigsen KB. Electric ships past, present, and future. J Power Sour 2014;255:341–54.
[6] Smogeli ØN. Ventilated thrusters in dynamic positioning mode control of marine propellers from normal to extreme conditions, PhD thesis. Trondheim (Norway): NTNU; 2006.
[7] Radan D. Integrated control of marine electrical power systems, PhD thesis. Trondheim (Norway): NTNU; 2008.
[8] Sørensen AJ, Smogeli ØN. Torque and power control of electrically driven marine propellers. Control Eng Pract 2009;17(9):1053–64.
[9] Smogeli ØN, Sørensen AJ. Antispin thruster control for ships. IEEE Trans Cont Syst Technol 2009;17(6):1362–75.
[10] Johansen TA, BØ TI, Mathiesen E, Veksler A, SØrensen AJ. Dynamic positioning system as dynamic energy storage on diesel-electric ships. IEEE Trans Power Syst 2014;29(6):3086–91.
[11] Bø TI, Johansen TA. Battery power smoothing control in a marine electric power plant using nonlinear model predictive control. IEEE Trans Control Syst Technol < http://ieeexplore.ieee.org/document/7558217/ > [in press].
[12] Hou J, Sun J, Hofmann H. Interaction analysis and integrated control of hybrid energy storage and generator control system for electric ship propulsion. In: American control conference; 2015. p. 4988–93.
[13] Hou J, Sun J, Hofmann H. Integrated control of power generation, electric motor and hybrid energy storage for all-electric ships. In: American control conference;

2016. p. 6797–802.
[14] Haseltalab A, Negenborn RR, Lodewijks G. Multi-level predictive control for energy management of hybrid ships in the presence of uncertainty and environmental disturbances. In: 14th IFAC symposium on control in transportation systems; 2016. p. 90–5.
[15] Zhang S, Xiong R. Adaptive energy management of a plug-in hybrid electric vehicle based on driving pattern recognition and dynamic programming. Appl Energy 2015;155:68–78.
[16] Zhang S, Xiong R, Cao J. Battery durability and longevity based power management for plug-in hybrid electric vehicle with hybrid energy storage system. Appl Energy 2016;179:316–28.
[17] Song Z, Hofmann H, Li J, Hou J, Han X, Ouyang M. Energy management strategies comparison for electric vehicles with hybrid energy storage system. Appl Energy 2014;134:321–31.
[18] Song Z, Hofmann H, Li J, Hou J, Zhang X, Ouyang M. The optimization of a hybrid energy storage system at subzero temperatures: Energy management strategy design and battery heating requirement analysis. Appl Energy 2015;159:576–88.
[19] Hebner RE, Davey K, Herbst J, Hall D, Hahne J, Surls DD, et al. Dynamic load and storage integration. Proc IEEE 2015;103(12):2344–54.
[20] Hou J, Sun J, Hofmann H. Mitigating power fluctuations in electric ship propulsion with hybrid energy storage system: design and analysis. IEEE J Ocean Eng < http://ieeexplore.ieee.org/document/7887693/ > [in press].
[21] D Park J, Kalev C, Hofmann H. Control of high-speed solid-rotor synchronous reluctance motor/generator for flywheel-based uninterruptible power supplies. IEEE Trans Indust Electron 2008;55(8):3038–46.
[22] Díaz-González F, Sumper A, Gomis-Bellmunt O, Bianchi FD. Energy management of flywheel-based energy storage device for wind power smoothing. Appl Energy 2013;110:207–19.
[23] Ren G, Liu J, Wan J, Guo Y, Yu D. Overview of wind power intermittency: impacts, measurements, and mitigation solutions. Appl Energy 2017;204:47–65.
[24] Spiryagin M, Wolfs P, Szanto F, Sun Y, Cole C, Nielsen D. Application of flywheel energy storage for heavy haul locomotives. Appl Energy 2015;157:607–18.
[25] Cheng M, Sami SS, Wu JZ. Benefits of using virtual energy storage system for power system frequency response. Appl Energy 2017;194:376–85.
[26] Kuseian J. Naval power system technology development roadmap. Electric Ships Office, PMS 320; 2013.
[27] Kulkarni S, Santoso S. Impact of pulse loads on electric ship power system: with and without flywheel energy storage systems. Electr Ship Technol Symp 2009:568–73.
[28] Elsayed AT, Youssef TA, Mohammed OA. Modeling and control of a low-speed flywheel driving system for pulsed-load mitigation in dc distribution networks. IEEE Trans Indust Appl 2016;52(4):3378–87.
[29] Hebner RE, Herbst JD, Gattozzi AL. Pulsed power loads support and efficiency improvement on navy ships. Naval Engin J 2010;122(4):23–32.
[30] Capasso C, Veneri O. Experimental analysis on the performance of lithium based batteries for road full electric and hybrid vehicles. Appl Energy 2014;136:921–30.
[31] Bolund B, Bernhoff H, Leijon M. Flywheel energy and power storage systems. Renew Sustain Energy Rev 2007;11(2):235–58.
[32] Aneke M, Wang M. Energy storage technologies and real life applications–a state of the art review. Appl Energy 2016;179:350–77.
[33] Luo X, Wang J, Dooner M, Clarke J. Overview of current development in electrical energy storage technologies and the application potential in power system operation. Appl Energy 2015;137:511–36.
[34] Zhang S, Xiong R, Cao J. Battery durability and longevity based power management for plug-in hybrid electric vehicle with hybrid energy storage system. Appl Energy 2016;179:316–28.
[35] Veneri O, Capasso C, Patalano S. Experimental investigation into the effectiveness of a super-capacitor based hybrid energy storage system for urban commercial vehicles. Appl Energy < https://doi.org/10.1016/j.apenergy.2017.08.086 > [in press].
[36] Zhang S, Xiong R, Sun F. Model predictive control for power management in a plug-in hybrid electric vehicle with a hybrid energy storage system. Appl Energy 2017;185:1654–62.
[37] Hou J, Sun J, Hofmann H. Battery/flywheel hybrid energy storage to mitigate load fluctuations in electric ship propulsion systems. In: American control conference; 2017. p. 1296–301.
[38] Carlton J. Marine propellers and propulsion, 3rd ed.; 2012.
[39] Rawson KJ. Basic ship theory, 5th ed.; 2002.
[40] O Suvire G, Molina MG, Mercado PE. Improving the integration of wind power generation into AC microgrids using flywheel energy storage. IEEE Trans Smart Grid 2012;3(4):1945–54.
[41] Chen M, Rincon-Mora GA. Accurate electrical battery model capable of predicting runtime and I-V performance. IEEE Trans Energy Convers 2006;21(2):504–11.
[42] Grbovic PJ. Ultra-capacitors in power conversion systems: applications, analysis and design from theory to practice, 1st ed.; 2013.
[43] Doucette RT, McCulloch MD. A comparison of high-speed flywheel, batteries, and ultracapacitors on the bases of cost and fuel economy as the energy storage system in a fuel cell based hybrid electric vehicle. J Power Sour 2011;196(3):1163–70.
[44] Song Z, Li J, Han X, Xu L, Lu L, Ouyang M, et al. Multi-objective optimization of a semi-active battery/supercapacitor energy storage system for electric vehicles. Appl Energy 2014;135:212–24.
[45] Wang C, Xiong R, He H, Ding X, Shen W. Efficiency analysis of a bidirectional DC/DC converter in a hybrid energy storage system for plug-in hybrid electric vehicles. Appl Energy 2016;183:612–22.
[46] Meinert M, Prenleloup P, Schmid S, Palacin R. Energy storage technologies and hybrid architectures for specific diesel-driven rail duty cycles: design and system integration aspects. Appl Energy 2015;157:619–29.
[47] Song Z, Hofmann H, Li J, Han X, Ouyang M. Optimization for a hybrid energy storage system in electric vehicles using dynamic programing approach. Appl Energy 2015;139:151–62.
[48] Yan D, Lu L, Li Z, Feng X, Ouyang M, Jiang F. Durability comparison of four different types of high-power batteries in HEV and their degradation mechanism analysis. Appl Energy 2016;179:1123–30.
[49] Geertsma RD, Negenborn RR, Visser K, Hopman JJ. Design and control of hybrid power and propulsion systems for smart ships: a review of development. Appl Energy 2017;194:30–54.
[50] Sun J. Optimisation-based control for electrified vehicles: challenges and opportunities. J Control Dec 2015;2(1):46–63.
[51] Camacho EF, Bordons C. Model predictive control, 2nd ed.; 2013.
[52] Rawlings JB, Mayne DQ. Model predictive control: theory and design, 1st ed.; 2009.
[53] Mayne DQ. Model predictive control: recent developments and future promise. Automatica 2014;50(12):2967–86.